1 **Gridded surface O₃, NOₓ, and CO abundances for model metrics from the South Korean ground station network**

2 Calum P. Wilson[1], Michael J. Prather[1]

3 [1]Department of Earth System Science, University of California (Irvine), Irvine, CA 92697, USA

4 *Correspondence to*: Calum P. Wilson (calumw@uci.edu)

5 **Abstract.** We present gridded surface air quality datasets over South Korea for three key species – ozone (O₃), carbon

6 monoxide (CO), and nitrogen oxides (NOₓ) during the timeframe of the Korea–US Air Quality (KORUS–AQ) mission (May–

7 June 2016). The tenth–degree hourly averaged abundances are constructed from the 300+ air quality network sites using

8 inverse distance weighting with simple declustering. Cross–comparing the interpolated fields against the site data that was

9 used to create them reveals high prediction skill for O₃ (80%) throughout South Korea, and moderate skill (60%) for CO and

10 NOₓ on average in densely observed regions after individual mean bias corrections. The gridded O₃ and CO interpolations

11 predict the NASA DC–8 observations in the planetary boundary layer (PBL) with high skill (80%) in the Seoul Metropolitan

12 Area (SMA) after subtracting the mean bias. DC–8 NOₓ observations were much less predictable on account of consistently

13 negative vertical gradients within the PBL. Our gridded products capture the mean and variability of O₃ throughout South

14 Korea, and of CO and surface NOₓ in most site–dense urban centres (SMA, Cheongju, Gwangju, Daegu, Changwon, and

15 Busan).

16 **1 Introduction**

17 Air quality control has become a priority in the Republic of Korea following an upward trend in ozone (O₃) pollution in all

18 major cities since the 1980s (Susaya et al., 2013). In May–June 2016, the Korea–US Air Quality (KORUS–AQ) mission was

19 launched with the goal of improving knowledge of the factors controlling Korean air pollution; this mission gathered extensive

20 observational data via aircraft, ground stations, ships, and remote sensing (Crawford et al., 2021).

21 Comparisons of modelled grid–cell values (i.e., averages) with point data from station sites remains awkward,

22 especially in high–emission environments with high sub–grid and temporal variability. Ground site comparisons in South

23 Korea have thus far used the arithmetic mean of sites within a grid cell or ungridded quantile analysis (Lennartson et al., 2018;

24 Peterson et al., 2019; Eck et al., 2020; Jordan et al., 2020; Schroeder et al., 2020; Park et al., 2021; Oak et al., 2022; Travis et

25 al., 2022), but these unweighted means can be biased by site clustering, and they lose information outside the cells. In this

26 work we develop a gridded dataset of key surface–level pollutants (in this case, O₃, NOₓ, CO) observed during the KORUS–

27 AQ timeframe. In contrast to arithmetic means, we apply Inverse Distance Weighting (IDW) interpolations (Shepard, 1968)

28 improved by Schnell et al. (2014) to create a country–wide continuous mapping of the National Institute of Environmental

29 Research (NIER) ground site data. We subsequently integrate the interpolated field over a 0.1°x0.1° grid. To evaluate the

interpolation, we predict NIER station measurements using the leave–one–out cross validation method; we predict observations from two research sites (Olympic Park and Taehwa Forest) to verify instrumental cohesion; and, we compare our gridded fields with DC–8 observations within the planetary boundary layer (PBL) to gauge how well the data products reproduce upper PBL abundances. In addition to providing gridded PBL datasets, we discuss the applicability and limitations of our methodology for each key species.

The observational data sets are described in Section 2, and the methods in Section 3. Results are summarized in Section 4. Conclusions and recommendations are presented in Section 5.

2 KORUS–AQ data

All KORUS–AQ datasets introduced in this section including the raw five–minute NIER station data are available via https://doi.org/10.5067/Suborbital/KORUSAQ/DATA01. The NIER station data is access–controlled, but we record our processed hourly–averaged NIER station data and our quality control flags for the raw data in our repository (see Wilson, 2024).

2.1 NIER air quality stations

The AirKorea monitoring network (https://www.airkorea.or.kr/eng) provided ground measurements of the key species averaged every 5 minutes at 323 stations across South Korea, of which 319 reported O_3, 311 reported CO, and 321 reported NO_x (Fig. 1). We calculate hourly median readings centred on the hour for each station, but omit clearly erroneous O_3 and NO_x dropouts from the average. High outliers exceeding five standard deviations above the mean of a weekly period were also discarded along with dropouts, which were manifest as stably low concentrations (1–4 ppb) persisting for multiple hours in stark contrast with the typical variability at the site. We were able to flag most dropouts algorithmically by analyzing the cumulative density functions (CDFs) of the station data partitioned into non–overlapping weekly intervals; improbably frequent low data often featured flat empirical gradients (less than 100th of the median CDF gradient) at the tail of the CDF. This technique proved insufficient at some stations however, and so we manually removed dropouts that were not flagged by our algorithm, as did Eck et al, 2020. The NIER instruments and procedures are not well documented and there remain some oddities: CO was reported with 1 ppb precision at 68 sites, and with 100 ppb precision at the remaining 250 sites.

2.2 Research stations

2.2.1 Olympic Park

The Olympic Park research station lies at the southeast edge of Seoul at 37.5216°N, 127.1242°E, 30 m above sea level, and served as a reference for ground–level Seoul pollution during the KORUS–AQ campaign (red star in Fig. 1). Hourly averages for the key species were recorded using NO_x–Ecotech EC9841, CO–Ecotech EC9830, and O_3–Ecotech EC9810 instruments (PI: Cho Seogu) during the KORUS–AQ period (10 May 01:00:00 to 18 June 00:00:00 LT). As Olympic Park station has four

60   proximal NIER stations within 5 km, reproducing this research station data from the NIER interpolation should be a test of the

61   small scale variability of Seoul pollution provided the instruments are well calibrated.

2.2.2 Taehwa Forest

63   The Taehwa Forest wilderness site lies 30 km southeast of Olympic Park at 37.3123°N, 127.3105°E and at 200 m elevation

64   (blue star in Fig. 1). It was used primarily to investigate the mixing of urban Seoul pollution with the biogenic volatile organic

65   compounds (BVOCs) of the forest. The three key species were measured by the existing NIER instruments (PI: Youngjae Li),

66   but supplemented by a Thermo Scientific 42i instrument for NO and a Cavity Ring–Down Spectroscopy for NO_2 (PI: Kim

67   Saewung, Kim et al., 2022).
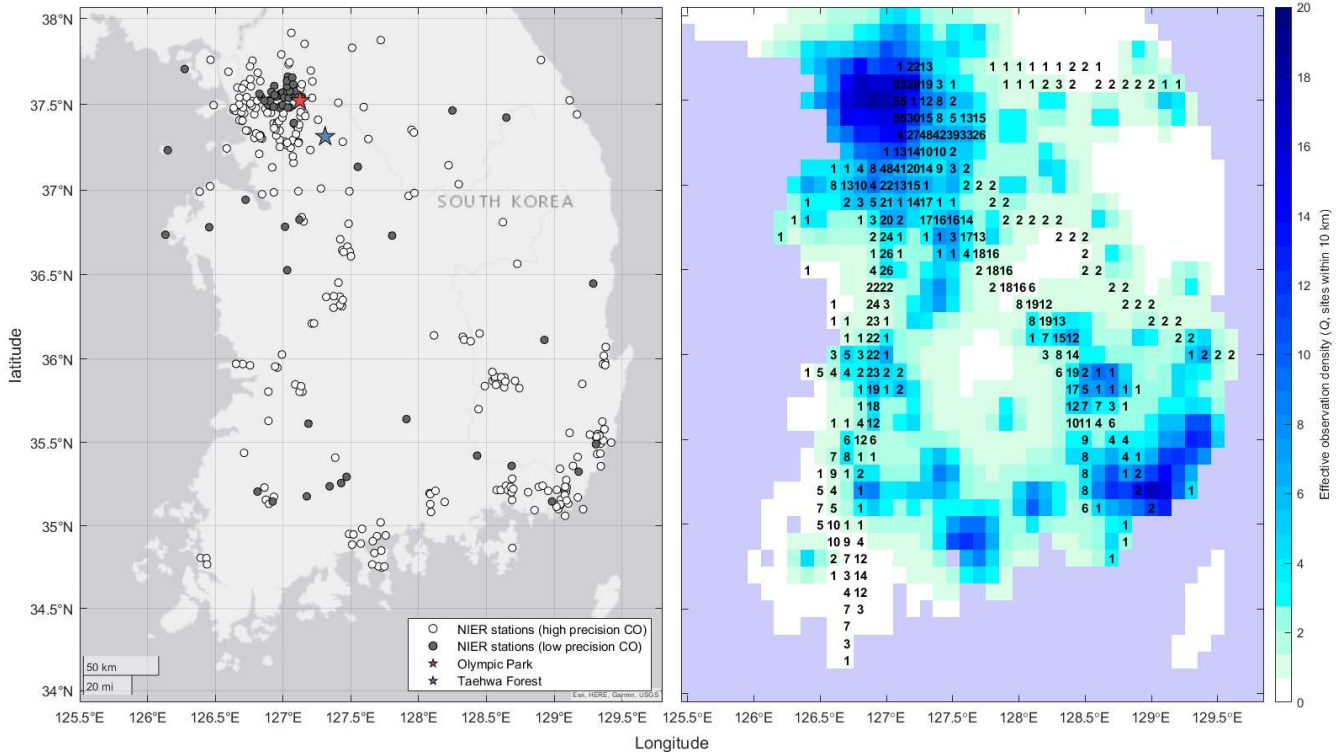
Figure 1: (**Left**) The geographical distribution of NIER ground stations and the two surface research stations operating during the KORUS–AQ campaign. High–precision stations (white circles) recorded CO at 1 ppb precision; low–precision stations (grey circles) recorded CO at 100 ppb increments. (**Right**) *Effective NIER station density (colour) within a 10 km radius* (Q, see Eq. (3)) gridded over 0.1°x0.1° cells. The number of contiguous DC–8 flight transects through each box in the PBL is printed in each cell. The aircraft radar altitude was evaluated against the ERA5 PBL height (based on hourly 0.25°x0.25° gridded data, Hersbach et al., 2023). The ERA5 data was interpolated in time to match the aircraft data.

2.3 NASA DC–8

76   The DC–8 aircraft routinely profiled the air over Taehwa Forest via loop manoeuvres in the morning and afternoon on flight

77   days between 2 May 2016 and 11 June 2016. It sampled other regions above South Korea and the Yellow Sea according to

78 pollution plume transport and cloud forecasts. We use the 10 s merged data our three key species: O_3, NO, and NO_2 were

79 measured with a 4–channel chemiluminescence instrument (Weinheimer et al., 1994); and CO, by Differential Absorption

80 Carbon monOxide Measurement (DACOM) (Sachse et al., 1991). We also use the 10 s data for latitude, longitude, radar

81 altitude, UTC time, and potential temperature (PI: Melissa Yang). From the DC–8 potential temperature measurements and

82 ERA5 surface data (Fig. A1) we can show that the ERA5 PBL heights accurately select DC–8 observations that are

83 adiabatically mixed from the surface (i.e., dθ/dz ~ 0), which is confirmed by the afternoon O_3 and CO profiles (Fig. A2). To

84 determine when the aircraft was in the PBL and thus could be compared with the interpolated surface map, we use the ERA5

85 PBL height data from reanalysis (hourly, 0.25°x0.25° grid, Hersbach et al., 2023). This approach is more accurate than simply

86 assuming that all DC–8 observations below 1.5 km radar altitude fall within the PBL (e.g., Oak et al., 2019).

87 **3 Methods**

88 Interpolation techniques compute an objective estimate $Z'(x,t)$ of a field $Z(x,t)$ at any geographic location x and time t as a

89 weighted mean of observations $Z_k(t)$ at stations indexed by k with weights $w_k(x)$:

90 $$Z'(x,t) = \sum_k [w_k(x)Z_k(t)] / \sum_k w_k(x) \qquad (1)$$

91 Ordinary Kriging and Inverse Distance Weighting (IDW) are two common interpolation methods that operate by this premise

92 but differ in how the station weights (w_k) are calculated (Matheron, 1963; Shepard, 1968). Kriging is a family of statistical

93 techniques based on the supposition that phenomena are autocorrelated in space, relying on an empirical distance–based

94 covariance model of $Z(x,t)$ determined from the station data. In our work we find minimal Pearson's correlation between

95 pairwise site covariance and proximity for any of the key species, so we opt for the modified IDW approach of Schnell et al.

96 (2014).

97   We examine the autocovariance functions of the sites to characterize the temporal variability of each key species at

98 five–minute resolution. The autocovariance function for a given phase shift (*e.g.* ten minutes) is defined as the covariance of

99 a time series of data with itself, but phase–shifted by ten minutes. The O_3 site autocovariance functions feature strong diurnal

100 cycles, preserving on average half of the respective site variances for a twenty–four–hour phase shift, compared with 35% for

101 CO and NO_x. Sub–ten–minute variability accounts for 3% of the O_3 site variance and 12% of the CO and NO_x variance on

102 average. Heterogeneous emissions and micrometeorology may be attributed to some of the CO and NO_x short timescale

103 variability seen in some Seoul sites and many CO–measuring sites in Gwangyang–Yeosu–Suncheon zone, while rural sites

104 suggest a possible instrumental noise component to the NO_x variability (See Fig. B of Appendix B).

105 **3.1 Inverse Distance Weighting**

106 In IDW techniques, weights are calculated from the reciprocal distances between estimation point x and the station coordinates

107 x_k, scaled by the exponent β. The greater density of observations in some regions creates a source of oversampling bias.

108 Schnell et al. (2014) address this clustering effect by reducing all station weights by M_k, the number of other stations within

109   distance D of site k, discounting sites with missing readings on an hourly basis.- In order to smooth the spatial heterogeneity

110   in $Z'(x,t)$ at small length scales, the distance D also serves as the minimum cutoff of $x-x_k$, and hence determines the

111   maximum weighting $w_k(x)$ of any nearby station. L is a maximum cutoff of $x-x_k$ used to reduce excess calculations for

112   extremely distant and unimportant sites. The weight formulae are summarized in Eq. (2):

113
$$w_k(x) = \frac{D^{-\beta}}{M_k} \qquad\qquad x - x_k \leq D$$

114
$$w_k(x) = \frac{(x-x_k)^{-\beta}}{M_k} \qquad\qquad D < x - x_k \leq L \qquad\qquad (2)$$

115
$$w_k(x) = 0 \qquad\qquad x - x_k > L$$

116   Our NIER station data consists of $k \in \{1, 2, \ldots, 323\}$ locations (Fig. 1) and $t \in \{1, 2, \ldots, 936\}$ hourly observations (10 May

117   01:00:00 to 18 June 00:00:00 LT) for each of our three key species (O_3, CO, NO_x) with some unreported or erroneous data.

118   We optimize β and D for each key species Z by randomly removing a fifth of the stations from the algorithm and then predicting

119   the abundance at each missing station k', adjusting each parameter until a 2D minimum was reached. In minimizing the total

120   root–mean–square error between predictions $Z'_{k'}(t)$ and observations $Z_{k'}(t)$ over the time series, we find similar optimal

121   values for each species ($\beta \sim 2$, $D \sim 5$ km, $L \sim 80$ km), with no significant improvement for larger L. The *effective density of*

122   *observations* $Q(x)$ is defined as the effective number of NIER sites within a 10 km radius of x in Eq. (3) (also called *Quality*

123   *of prediction*, Eq. (5) of Schnell et al., 2014). We expect Q to correlate with prediction accuracy:

124
$$Q(x) = 10^\beta \sum_k w_k(x) \qquad\qquad (3)$$

125   Compared with the arithmetic mean gridding, the gridded IDW observations show no significant mean bias. However,

126   significant mean absolute deviations can be seen in the densely observed ($Q > 10$) Seoul Metropolitan Area and Southeast

127   coastal cities. In such regions, the mean absolute deviations for O_3, CO, and NO_x are 5 ppb, 58 ppb, and 9 ppb respectively.

128   Conversely, the most sparsely measured regions show the best agreement between the two methods due to mutual sampling

129   of a single station. Both methods are fundamentally limited by sampling density, particularly in urban centres with high

130   spatial emission variability. The differences seen in the most densely observed regions highlight the instability of the

131   arithmetic mean method with respect to grid size and boundary manipulation.

132   **3.2 Statistical techniques**

133   To evaluate the accuracy and predictive capability of an interpolation, we examine the error $E(t)$ in a time series of predictions

134    $Pre(t)$ and observations $Obs(t)$ at a given location for a given species with all time points equally weighted equally. We

135   calculate a sequence of three error series defined as follows:

136
$$E1(t) = Pre(t) - Obs(t)$$

137
$$E2(t) = Pre(t) - Obs(t) - (\overline{Pre(t)} - \overline{Obs(t)}) \qquad\qquad (4)$$

138
$$E3(t) = b\,Pre(t) - Obs(t) - (b\,\overline{Pre(t)} - \overline{Obs(t)})$$

139   Where $E1(t)$ is the absolute error in the predictions, $E2(t)$ is the error after correcting for the mean prediction bias $(\overline{Pre(t)} - $

140    $\overline{Obs(t)})$ and $E3(t)$ is the error relative to a simple linear regression (LR) model of $Pre(t)$ vs. $Obs(t)$ fitted by ordinary least

141   squares, i.e., after correcting for mean bias and slope (b). We then apply the *coefficient of determination* to compute the fraction

142   of the observed sample variance, $Var(Obs(t))$, explained by e.g. the raw predictions ($E1(t)$):

143
$$R^2{}_{E1} = 1 - \frac{Mean(E1(t)^2)}{Var(Obs(t))} \tag{5}$$

144   And do similarly for $E2(t)$ and $E3(t)$. $R^2{}_{E1}$ is a *predictive accuracy* statistic that ranges from minus infinity to one and is

145   identical to the forecast skill score referenced to the mean of observations (Murphy, 1988). $R^2{}_{E2}$ describes how well the

146   predictions capture the temporal variability in the observations regardless of any mean bias and has the same range as $R^2{}_{E1}$.

147    $R^2{}_{E3}$ is the common definition of R^2 in regression analysis and ranges from zero to one due to the fitting constraint. $R^2{}_{E3}$

148   describes the *predictability* of the observations from the LR model regardless of any difference in the mean or variance of

149    $Pre(t)$ and $Obs(t)$. A score of zero for a given $R^2{}_E$ is equivalent to predicting a static mean of observations across the time

150   domain. The maximum score for $R^2{}_{E1}$ and $R^2{}_{E2}$ is limited by the interpolation variance, which is typically damped relative to

151   the contributing stations, especially in regions with highly heterogeneous emissions. Figure 2 (right–hand side) suggests the

152   average station predictability ($R^2{}_{E1}$ and $R^2{}_{E2}$) score has an upper bound of around 0.9 for O_3 and 0.8 for CO and NO_x.

153   **3.2.1 Leave–one–out cross validation.**

154   In this trial, we sequentially remove each station k, then interpolate (predict) its value from the remaining stations: $Pre(k, t) = $

155    $Z'(k, t)$, where $Obs(k, t) = Z(k, t)$ (see Eq. (4); Brauer et al, 2003; Hochadel et al., 2006). A perfect interpolation would

156   accurately reproduce the mean and standard deviation of the measurements, indicating (1) no mean bias error and (2)

157   preservation of daily maximae and minimae. Our optimized IDW interpolation has clearly worked well in terms of mean bias

158   (left half of Fig. 2). The box quartiles and non–outlier whiskers (i.e., the full range of values within one–and–a–half

159   interquartile ranges from the outer quartiles) are well centred on zero bias, with the spread broadening from O_3 to CO to NO_x.

160   The symmetry of the whiskers comes from the case where two sites, distant from the remaining sites but near one another, are

161   the only sites used to interpolate one another and hence if one site has twice the mean value of another, we get symmetric plus–

162   minus biases for each site. The median of the mean NO_x site biases is +13%, and this appears to be an artefact of low NO_x

163   abundances in rural ($Q < 5$) locations. The absolute mean NO_x bias averages –0.6 ppb (urban –3.0 ppb, rural +6.5 ppb).

164   Incoherence among nearby urban stations combines to dampen the interpolation variability, especially for CO and NO_x, which

165   feature independent high spatial variability from local sources. This is shown on the right half of Fig. 2, where most of the

166   standard deviation ratio quantiles lie below unity. We believe this reduced standard deviation in the prediction time series

167   better represents the average over a grid cell that contains several incoherent sites.

168
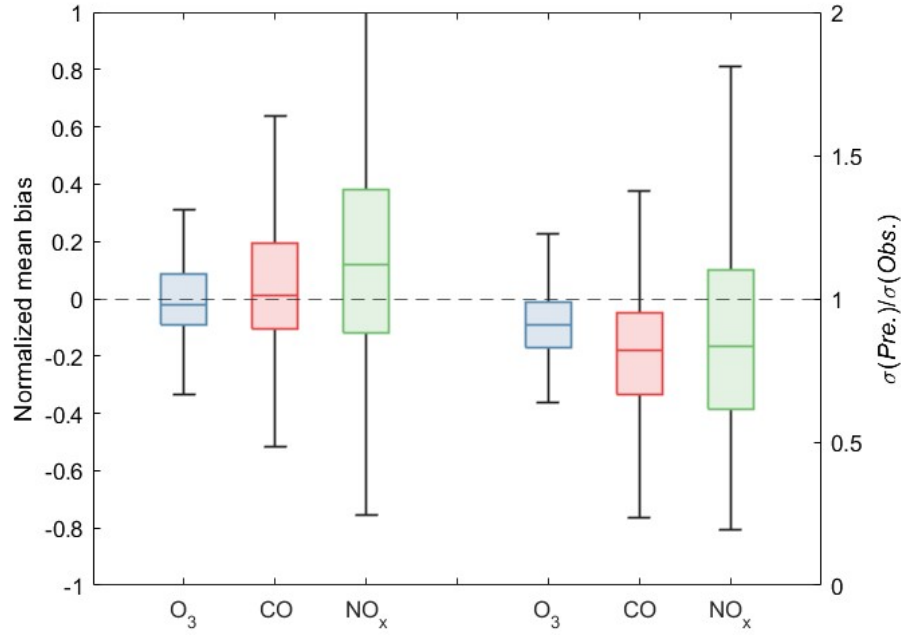
Figure 2: (left) Box plots of normalized mean bias: $NMB(k) = Mean(Pre(k, t) - Obs(k, t))/Mean(Obs(k, t))$ and **(right)** standard deviation ratio $\sigma(Pre(k, t))/\sigma(Obs(k, t))$ for interpolated time series at each NIER site using leave–one–out cross validation. Whiskers show the range of non–outliers, where outliers are data beyond one–and–a–half interquartile ranges from the outer quartiles. Results are shown for O_3 (blue), CO (red), and NO_x (green). Mean bias is normalized by the observed mean, and the ratio of standard deviations is analogous to the gradient of a linear regression.

The sequence of R^2_E scores ($E1$–3) for each site and each species are shown in Fig. 3. The O_3 scores (top row) are consistently high across the sequence. R^2_{E1} through R^2_{E3} scores for O_3 indicate that the O_3 interpolation was accurate and unbiased at almost all NIER stations in South Korea. For CO (middle row) and NO_x (bottom row), there is an improvement in absolute prediction accuracy (R^2_{E1}) as the density of observations (Q) increases, and further improvement after correcting the mean bias in the predictions (R^2_{E2}). The linear regression models (R^2_{E3}) offer an obvious improvement to predictability in rural regions (low Q) where information is lacking, but no significant improvement in well sampled urban regions (high Q). With no large net mean bias for any key species (Fig. 2), we assert that the average of our interpolations should capture the mean and possibly the variability of a well–mixed gridded domain. We test this assertion later using aircraft PBL observations averaged into 0.1°x0.1° cells. The high range of R^2_E values for NO_x and CO, even where $Q > 10$, suggests that absolute mean error in the prediction is a problem for many sites, implying they are driven by very small scale (<1 km) local emissions in contrast to O_3, which is not emitted directly. For NO_x, the sequence from $E1$ to $E2$ greatly improves the prediction accuracy. For CO, there remains a large fraction of unpredictable sites, often with very high standard deviations (dark red circles), implying large nearby emissions. Figure 4 (top–middle and top–right panels) shows the clustering of such sites for CO and NO_x in Daejeon (central–western South Korea) and in the southern coastal cities of Gwangyang, Yeosu, Suncheon, Jinju, and Ulsan (no NO_x data). When we

189   compare the LOOCV performance of NO_x with the complete interpolation (*i.e.*, no stations omitted, see bottom panel of Fig.

190   4), we see R^2_{E2} scores change by > 0.4 at *e.g.* rural sites, the Busan shoreline, and the manufacturing district sites of Northern

191   Yeosu and Eastern Gwangyang. These discrepancies indicate under–sampling of NO_x across rural South Korea and in some

192   urban districts with locally contrasting emission activity.

193
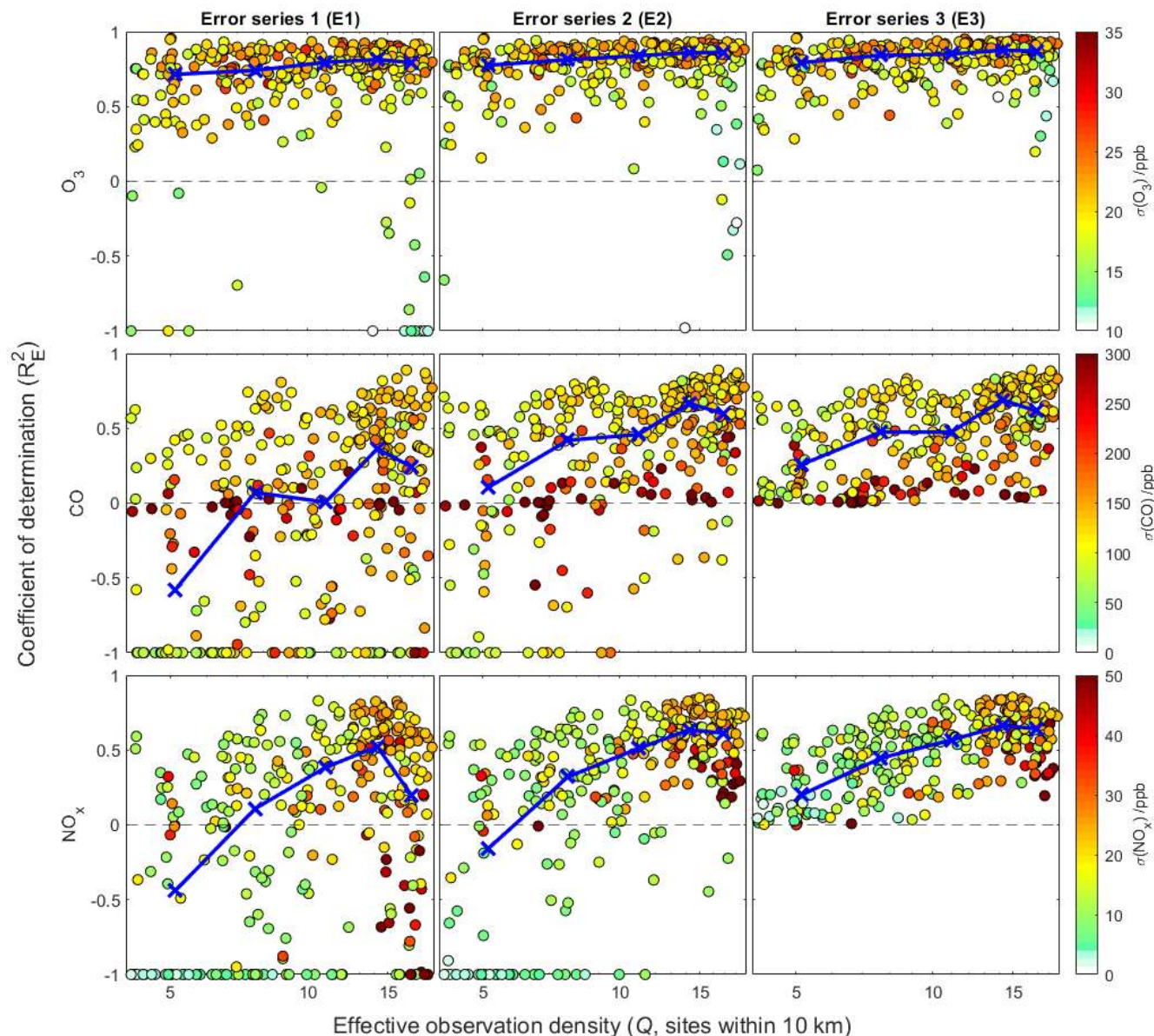
Figure 3: Generalized coefficient of determinations (R^2_E, Eq. (5)) for NIER station predictions vs. the effective density of
nearby observations (Q, effective number of sites in a 10 km radius). The three columns show the sequence R^2_{E1}, R^2_{E2}, and
R^2_{E3}. The three rows are for the species O_3 (**top**), CO (**middle**), and NO_x (**bottom**). The calculations use the leave–one–out
cross validation at each NIER station (circles) coloured by the standard deviation of observations. The blue conjoined crosses
show the median R^2_E values for five percentile partitions of Q: 0–20%, 20–40%, 40–60%, 60–80%, and 80–100%.

199
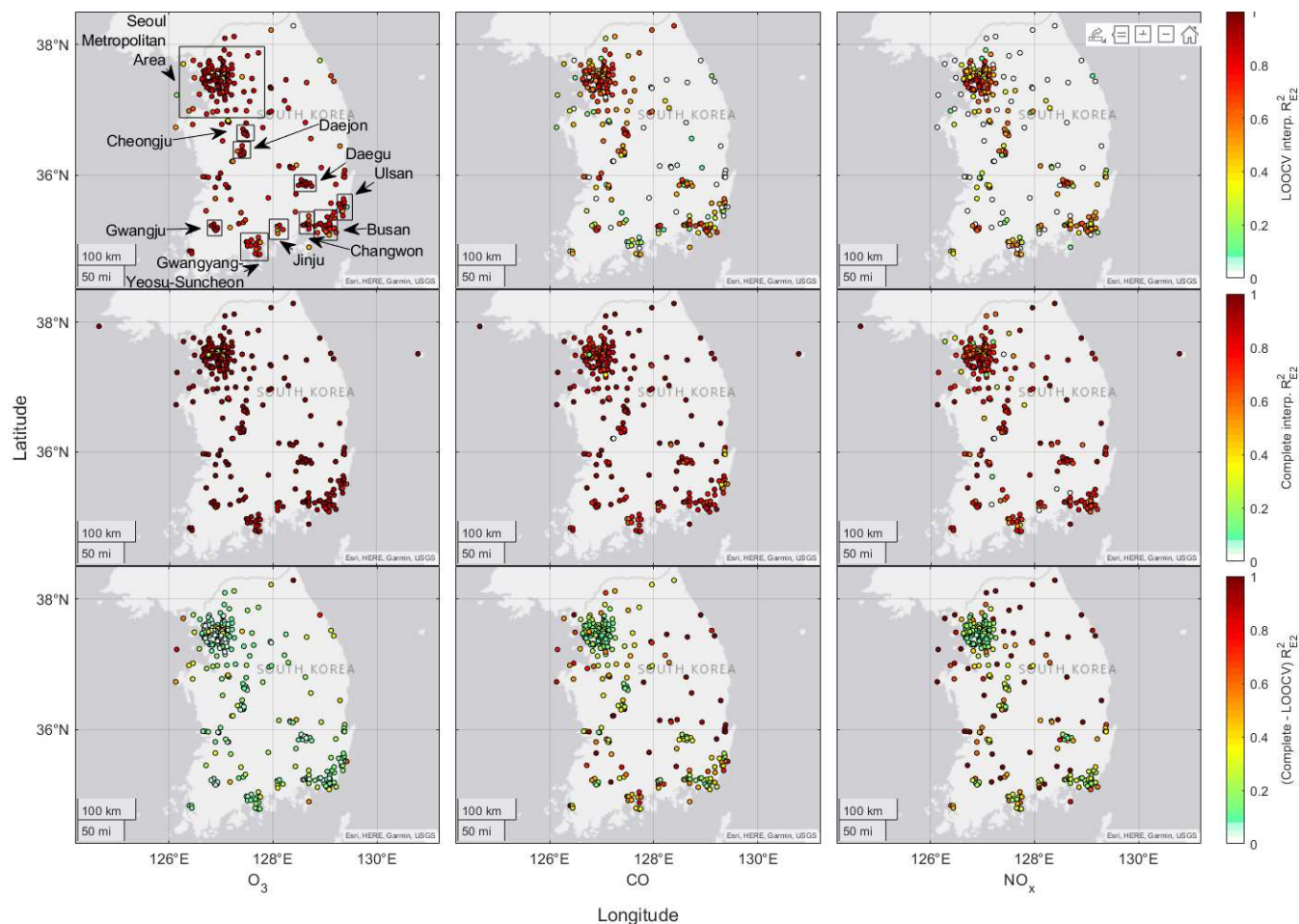
Figure 4: The geographical distribution of NIER station prediction accuracies with the mean prediction bias removed from each station (R$^2_{E2}$, Eqs. (4) and (5)), shown for the three key species: O$_3$ (**left**), CO (**middle**), and NO$_x$ (**right**). **Top:** R$^2_{E2}$ scores for the LOOCV interpolations. **Middle:** R$^2_{E2}$ scores for the complete interpolation, *i.e.* without omitting the data from predicted sites. **Bottom:** The difference between the complete– and LOOCV– interpolation R$^2_{E2}$ scores. Negative R$^2_{E2}$ values are truncated to zero. Approximate city bounds are shown via text and boxes in the top–left panel.

We have additionally compared the interpolation accuracy during the four meteorological phases presented by Peterson et al. (2019), *i.e.*, dynamic, anticyclone, low–level transport, and rex blocking, although we did not identify any obvious patterns across the phases (see Fig. C1 of Appendix C). An alternative test of meteorological influence is daytime (07:00 to 20:00 LT) *vs.* nighttime (21:00 to 06:00 LT) predictability, *i.e.*, prevailingly turbulent *vs.* stably stratified atmospheric surface conditions. Ozone and NO$_x$ showed greater LOOCV predictability (R$^2_{E2}$) during daytime than nighttime by around +0.1 and +0.05 respectively, but not CO (see Fig. C2). More efficient turbulent mixing during daytime vs. nighttime likely smoothed some of the small–scale emission heterogeneity, resulting in more predictable fields.

3.3 Gridded air quality data

A major objective of this study was to obtain grid–cell averages (0.1°x0.1°, approx. 10 km x 10 km) for testing regional air quality models. Within each 0.1°x0.1° cell, we interpolate the key species to twenty–five points on a 0.02°x0.02° grid centred in the cell, and then average these values. The averages do not account for latitudinal differences in quadrangle areas, which are minor for South Korean latitudes. We apply the same treatment to the density of observations to produce the gridded Q values as seen in Fig. 1 (right–hand side).

3.4 Aircraft cell averages

We collect the measurements of O_3, CO, and NO_x from NASA DC–8 taken over land at radar altitudes below the PBL heights taken from the ERA5 data. The DC–8 measurements used here are 10 second merges corresponding to approximately 1 km flight segments $S \in \{1, 2, \ldots, 13942\}$. To compare the segments with the gridded site data, we average the contiguous segments through each grid cell to produce transect–averaged observations $Obs(T)$, where transects $T \in \{1, 2, \ldots, 2106\}$ contain around seven segments whose midpoints lie in the cell bounds. For the prediction set $Pre(T)$, we interpolate the traversed cells in time to match the mean aircraft time of flight during the respective transects. The number of transects through each cell is indicated by the gridded numbers in Fig. 1 (right–hand side).

4 Results

Table 1: The generalized coefficients of determination R^2_{E1}, R^2_{E2}, and R^2_{E3} (Eq. (5)) for predictions vs. measurements at research stations (Olympic Park and Taehwa Forest) and along flight transects in the PBL. Each flight transect is a median of contiguous 10 s observations through a grid cell (See Fig. 1 for sampling distribution and Fig. 5 for scatter plots), and the predictions are gridded values interpolated linearly in time to match the aircraft time of flight, then averaged. $E1$, $E2$, and $E3$ are time series of prediction errors defined in Eq. (4). NO_x measurements at Taehwa Forest are taken from Kim et al., 2022.

Species	Olympic Park			Taehwa Forest			DC–8 (all transects)			DC–8 ($Q > 10$ transects)		
	R^2_{E1}	R^2_{E2}	R^2_{E3}	R^2_{E1}	R^2_{E2}	R^2_{E3}	R^2_{E1}	R^2_{E2}	R^2_{E3}	R^2_{E1}	R^2_{E2}	R^2_{E3}
O_3	0.90	0.92	0.96	0.68	0.82	0.82	0.02	0.69	0.69	0.26	0.81	0.90
CO	0.73	0.75	0.76	–2.70	0.69	0.71	–2.20	0.28	0.41	–0.91	0.83	0.84
NO_x	0.67	0.68	0.68	–12.0	–3.60	0.00	–2.60	0.34	0.62	–0.84	0.51	0.73

4.1 Research site prediction

Research stations provide case studies where the quality of measurements is carefully controlled, and so instrumental drift, noise, and biases are minimized. For each key species, we compare the NIER station data interpolated to the coordinates of the research stations, either at Olympic Park or Taehwa Forest, against the research station instruments (Fig. 5). Olympic Park and Taehwa Forest have effective sampling densities (Q) of 16 and 6 stations per 10 km respectively. Figure 5 shows accurate

240   prediction of O_3 at both sites with predictably more scatter at Taehwa Forest where less information was available. We see a
241   similar pattern for CO, but with a mean bias (predicted NIER interpolated value minus research instrument measurement) of
242   +100 ppb at Taehwa Forest. NO_x is predicted reasonably well at Olympic Park except in the highest measured range (>100
243   ppb), but predictions appear random at Taehwa Forest. Table 1 indicates excellent prediction accuracy at Olympic Park for all
244   species (R^2_{E1}), and at Taehwa Forest for O_3. At Taehwa Forest, CO prediction improves when mean biases are removed (R^2_{E2}),
245   but NO_x remains unpredictable. The linear regressions (R^2_{E3}) lead to very little improvement over mean bias correction (R^2_{E2}),
246   implying that the temporal variability measured by the research stations was well captured. High R^2_{E1} scores suggest good co–
247   calibration between the Olympic Park instruments and surrounding NIER instruments. We are unable to characterize the mean
248   biases at Taehwa Forest.
249   As an isolated wilderness site, Taehwa Forest presents a unique problem for interpolating NO_x values based on NIER
250   stations. The closest three NIER sites surround the forest station at a distance of around 10–15 km, and all are subject to NOx
251   roadside emissions, thus our interpolation maps these high–NOx values into the relatively NOx–depleted forest.

252
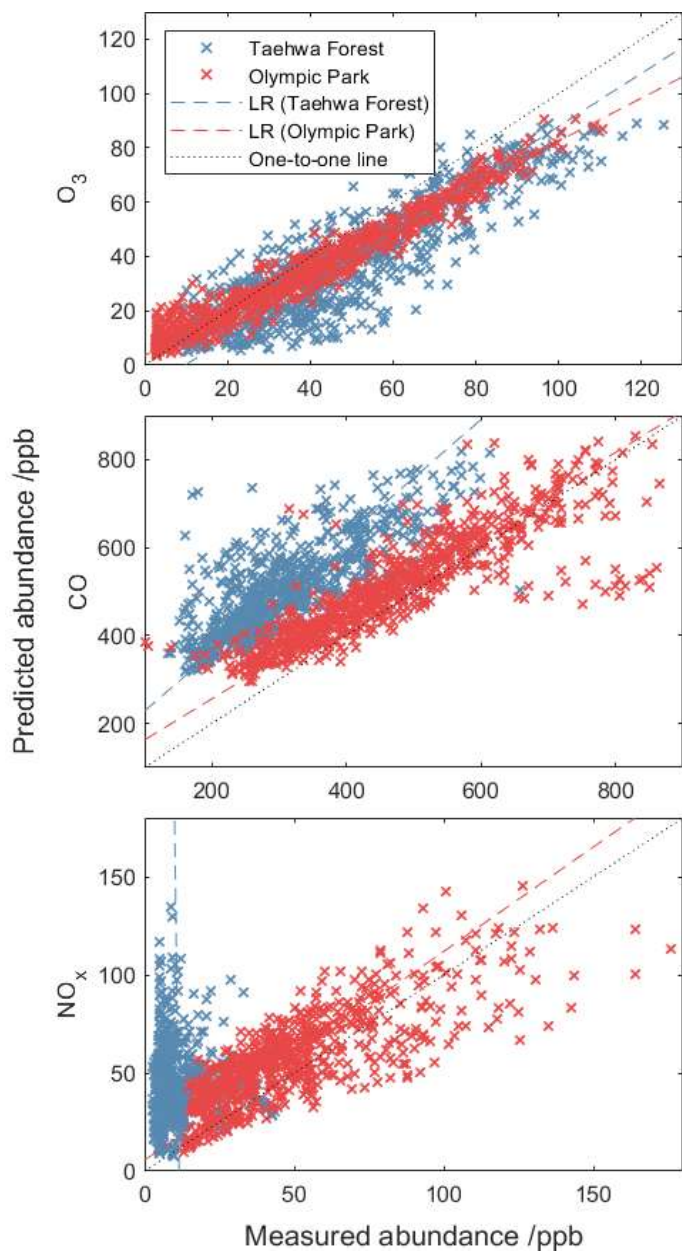
Figure 5: Predicted vs. measured abundances of the three key species at Olympic Park (red) and Taehwa forest (blue) research
stations. Predicted abundances are computed as point interpolations as per Equation (1). Dashed lines are linear regression
(LR) models fitted by ordinary least squares.

4.2 DC–8 comparison

Figure 6 (top panel) shows that the gridded surface–site predictions of the DC–8 O_3 observations are consistently lower than

observed but remain strongly correlated. CO predictions (Fig. 6, middle panel) show a consistent bias of around +100 ppb, but

259   otherwise capture the variability of the aircraft CO measurements reasonably well. NO_x predictions (Fig. 6, bottom panel)

260   show a consistent positive bias along with randomness in the low measured range (<10 ppb). The gridded O_3 and CO

261   predictions are highly accurate (R^2_{E2} = 80%) in grid cells with effective observation density (Q) exceeding ten, mainly sampled

262   in the Seoul Metropolitan Area (Fig. 1, right–hand side). These findings show that with enough ground information, our

263   gridded O_3 and CO datasets can predict upper PBL variability even in regions with intense small–scale emission heterogeneity.

264   NO_x is exceptional, however, due to the rapid fall–off in abundance with altitude even within the PBL (Fig. A2 of Appendix

265   A, see also Fig. 2 from Kim et al., 2021). We believe that O_3 titration in the Seoul Metropolitan Area also leads to a slight

266   underestimation in predicted variability as, shown by a 10% increase in predictability using linear regression (R^2_{E3} = 90%,

267   Table 1). We note however that the recurring flight patterns did not uniformly sample our grid domain and may have over– or

268   under–sampled some sub-grid regions. Obtaining vertically averaged concentrations rather than surface values remains a

269   challenge given the substantial near–surface gradients inferred from Figs. 6 and A2, and suggests the need for vertically

270   resolved chemical and dynamical modelling.

271
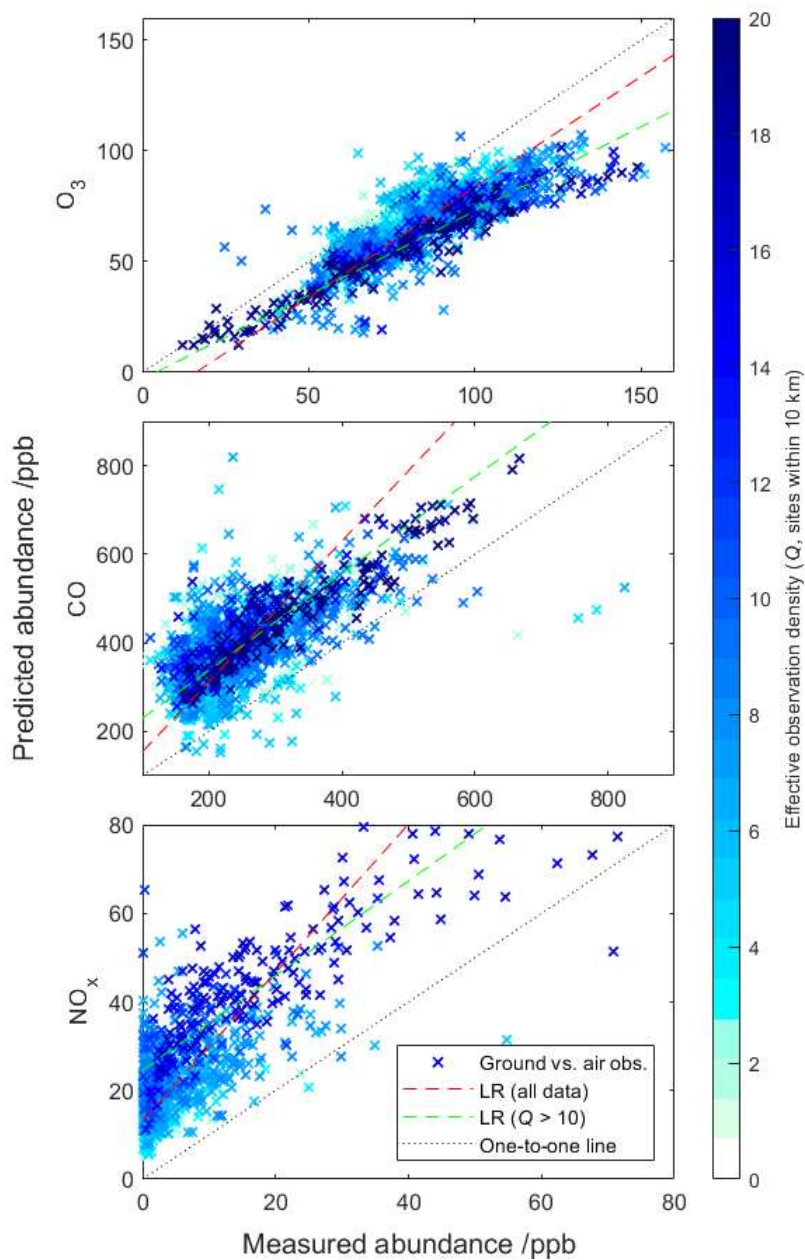
Figure 6: Comparison of 10 s DC–8 observations in the PBL and gridded (0.1°x0.1°) hourly ground station data. Each data
point represents the median of the contiguous aircraft transect through a grid cell (y–axis) and the median of the gridded ground
station data interpolated linearly in time to match the aircraft time of flight (x–axis).

5 Conclusions

We create gridded (0.1°x0.1°) observational datasets from NIER ground station measurements of air quality over South Korea. Unlike the arithmetic mean gridding technique, t~~T~~his~~e~~ method includes information from all nearby stations, including those outside the cell boundary, while mitigating sampling bias from site clustering~~.~~. We identified significant mean absolute deviations between the IDW and arithmetic mean gridding techniques in *e.g.* the Seoul Metropolitan Area where IDW was most proved most accurate, prompting caution on the use of arithmetic mean gridding.

Our results suggest that the mean and variability of ground level O_3 was well captured over the whole of South Korea. For CO and NO_x, our LOOCV analysis revealed mean biases in certain NIER site predictions, but otherwise good prediction accuracy in most densely observed urban regions after the biases were subtracted. The well–predicted regions include the Seoul Metropolitan Area, Busan, Changwon, Daegu, and Cheongju, whereas prediction accuracy was poorer in the conjoined coastal cities of Gwangyang, Yeosu, and Suncheon, and in Ulsan; predictability in these regions would benefit from denser sampling. The aircraft comparisons confirm that the variability of O_3 and CO in the PBL are well captured from the surface stations; however, NO_x vertical gradients in the PBL confound attempts to predict the aircraft NO_x measurements.

Inverse Distance Weighting is susceptible to errors from over– or under–sampling of intense emission sources such as roadsides and industrial sectors. The characteristic concentrations of these regions may also be projected beyond the reach of the emission sources as seen in the high CO and NO_x biases at Taehwa Forest. These error sources are not unique to IDW. Nevertheless, improvements in NO_x predictability might be found with Land–Use regression and Machine Learning approaches as reviewed by Karroum *et al.* (2020), although these are outside the scope of the present paper. Such techniques can account for reactive NO_x decay away from sources, potentially mitigating errors from source–sampling bias and over–projection. It would be interesting to compare the site predictabilities *vs.* sampling density for these alternate techniques, particularly in regions that were under–sampled according to LOOCV.

6 Appendices

308

Appendix A

309

310
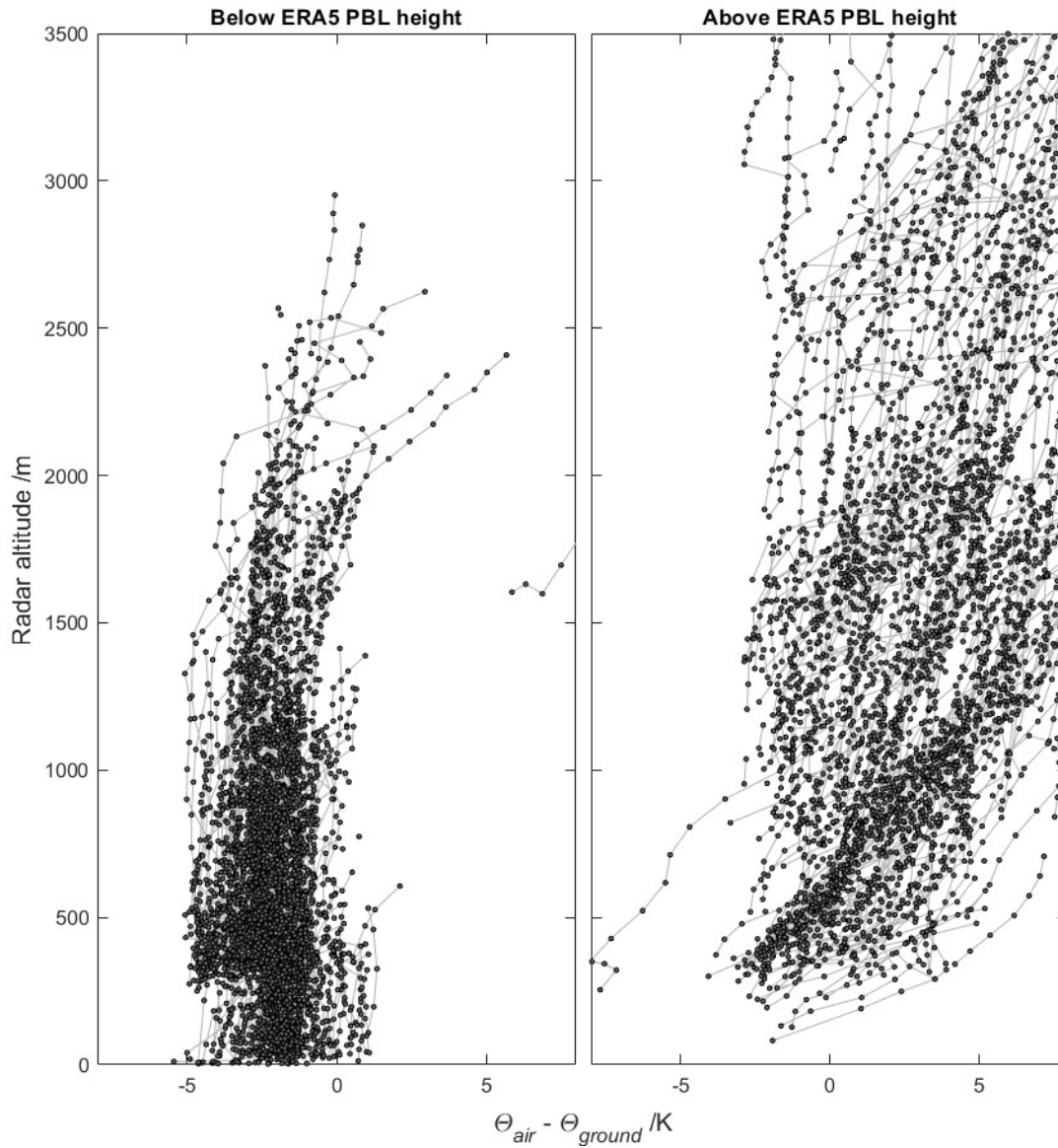
Figure A1: DC–8 10 s potential temperature (θ_{air}) measurements (dots) in a half degree radius of Taehwa Forest research
station with gridded (0.25°x0.25°) surface potential temperature (θ_{ground}) subtracted, taken below (**left**) and above (**right**) the
ERA5 designated PBL height. Lines connecting dots indicate contiguous transects, and all data was taken during ascent or
descent (aircraft vertical speed > 1 m s^{-1}). θ_{ground} was calculated using the ERA5 2 metre temperature and surface pressure
fields at native resolution (0.25°x0.25°, hourly), interpolated in time to match the aircraft time of flight.

311
312
313
314
315
316
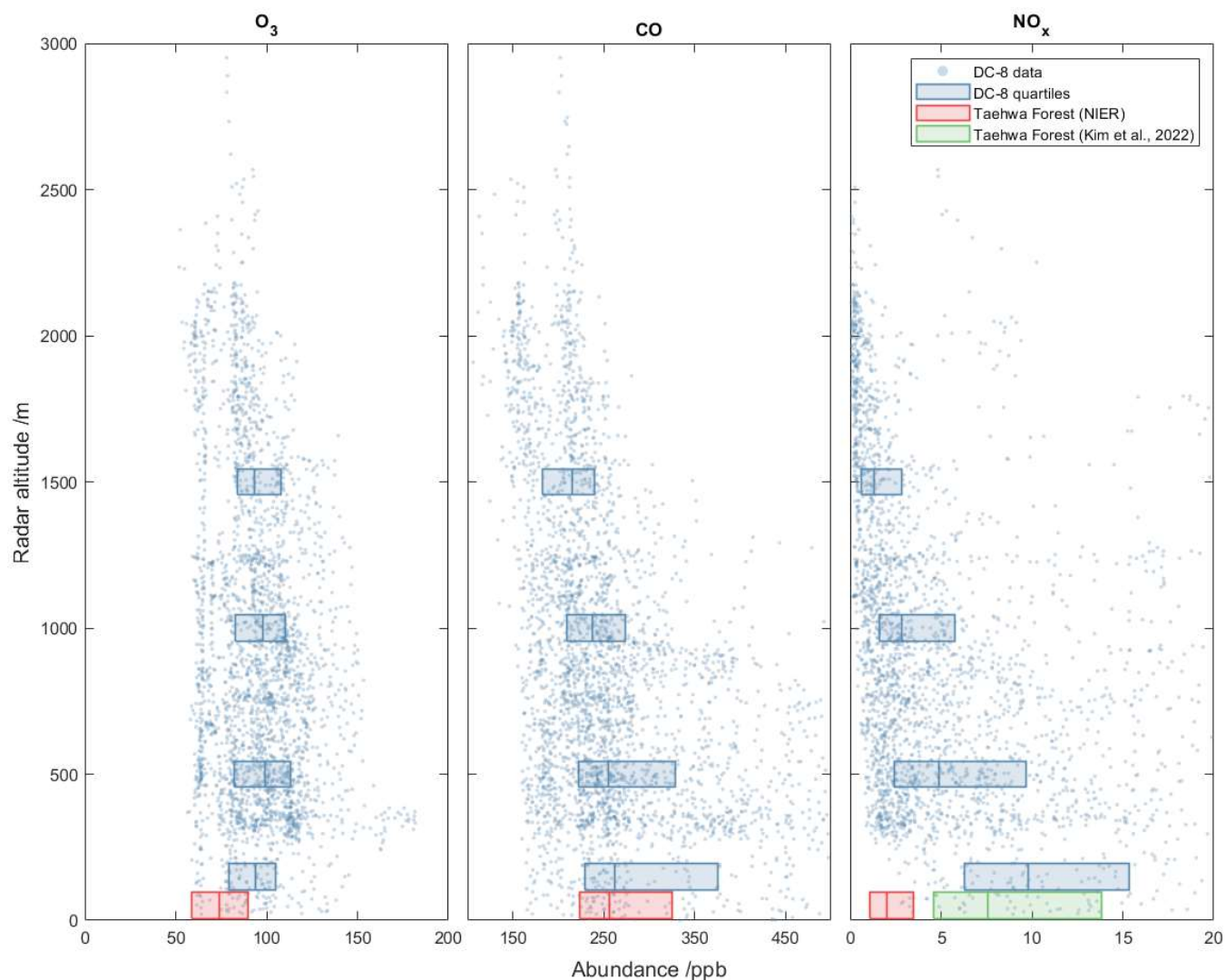
317
Figure A2: Vertical profiles of the DC–8 measured O_3 (**left**), CO (**middle**), and NO_x (**right**) in the ERA5 PBL within a half
degree radius of Taehwa Forest research station. All data is sampled between the hours of 12:00 and 17:00 LT, and quartiles
are shown for aircraft data (blue) partitioned into altitude bins (0–250, 250–750, 750–1250, and 1250–1750 m) and for the
available ground research station measurements at Taehwa Forest (red) supplemented by Kim et al., 2022 (green).

322
323

324

325

326

327

328

329
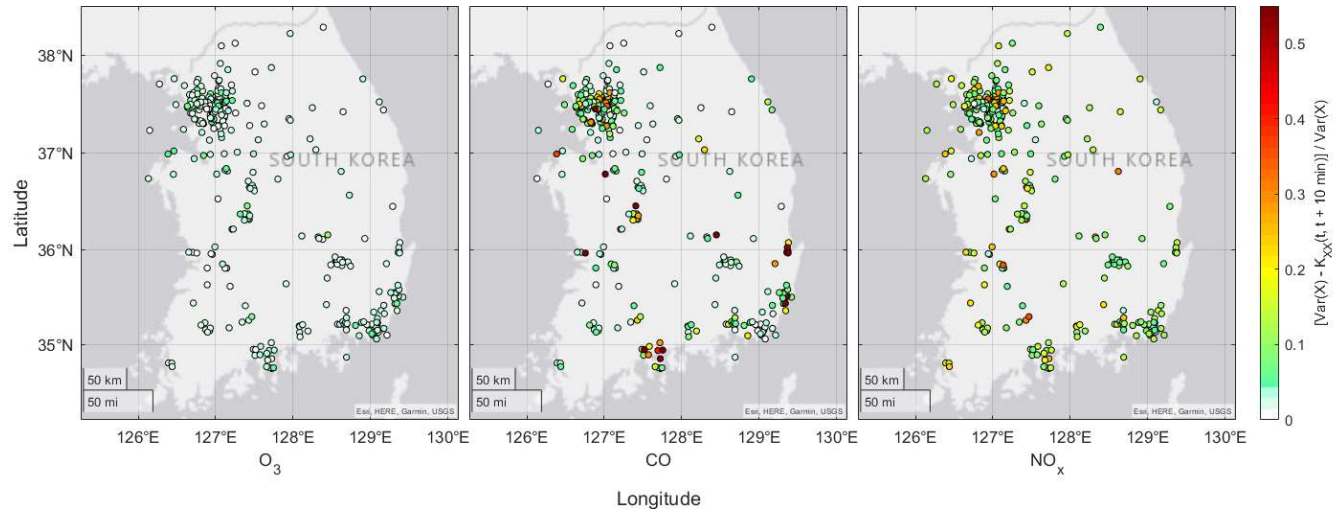
331
Figure B: The sub–ten–minute temporal variability of the quality–controlled O_3 (**left**), CO (**middle**), and NO_x (**right**) site data
at five–minute resolution. Sub–ten minute variability for individual sites was calculated as the site autocovariance subject to a
ten–minute phase shift ($K_{XX}(t, t + 10 \text{ min})$) subtracted from the total site variance ($\text{Var}(X)$), normalized by $\text{Var}(X)$.

335

336

337

338

339

340

341

342

343

344

345

346

347

348

349

350

351

352

353

354
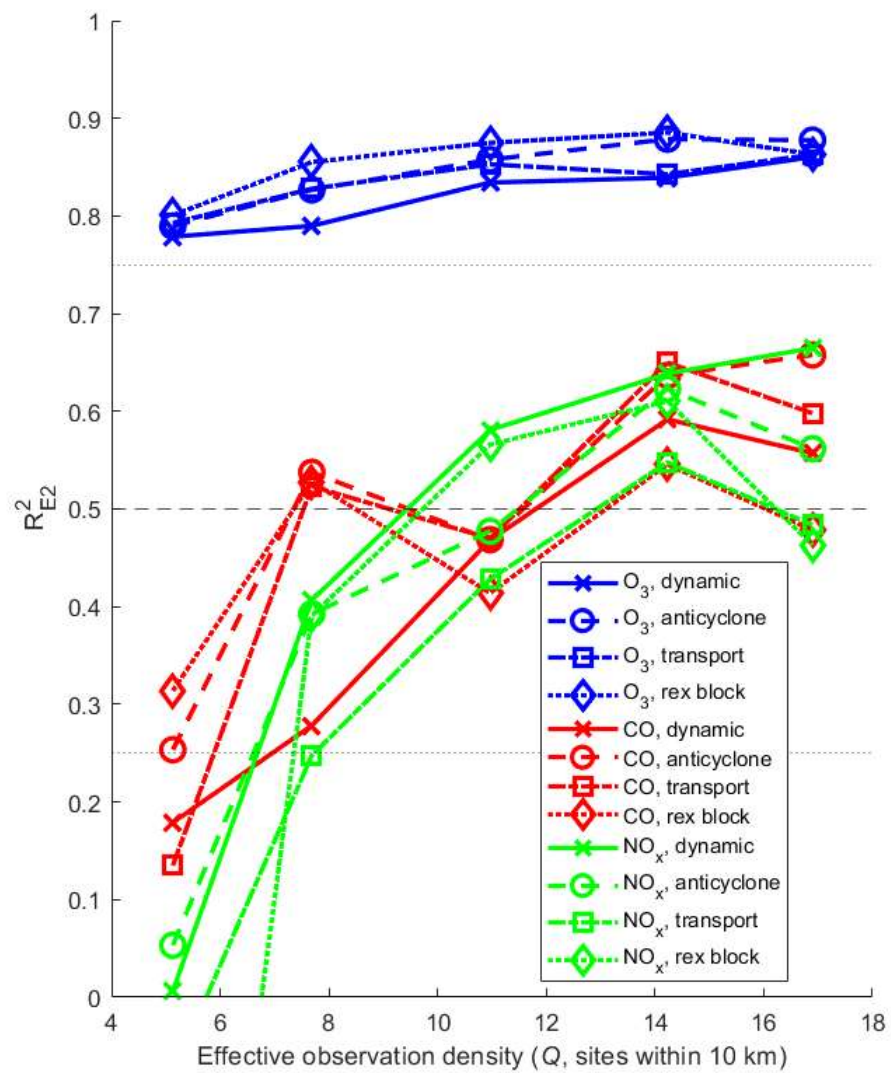
356
357   **Figure C1:** The median prediction accuracy (R^2_{E2}) of O_3 (**blue**), CO (**red**), and NO_x (**green**) within percentile bins (0–20%,
358   20–40%, 40–60%, 60–80%, and 80–100%) during the meteorological phases (dynamic, anticyclone, transport, and rex
359   blocking) described by Peterson *et al.* (2021).
360
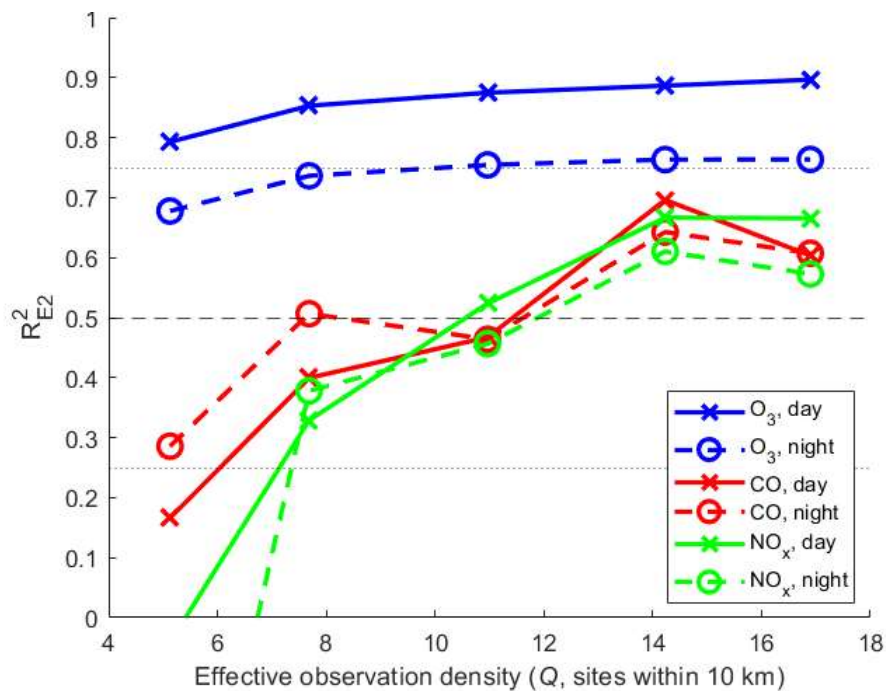
361
362 **Figure C2:** As in Fig. C1, but for daytime (07:00 to 20:00 LT incl.) and nighttime (21:00 to 06:00 LT incl.) data.

363 **Data Availability**

364 Gridded data products and the datasets used in analysis are available from Wilson, 2024:

365 https://doi.org/10.5061/dryad.sf7m0cgf5.

366 **Author contribution**

367 CW wrote the code to produce the datasets, codesigned and performed the analysis, ~~and~~ drafted ~~prepared~~ the manuscript, and

368 responded to the reviews. MP designed the methodology, codesigned the analysis, reviewed and edited the manuscript.

369 **Competing interests**

370 The authors declare that they have no conflict of interest.

Acknowledgements

This study was funded by NASA (# 80NSSC21K1454) and the National Science Foundation (NSF, # AGS-2135749). We acknowledge NASA and NIER for providing the trace gas data used in this study and we are grateful to Kim Saewung for guidance on the KORUS–AQ data usage.

References

Brauer, M., Hoek, G., van Vliet, P., Meliefste, K., Fischer, P., Gehring, U., Heinrich, J., Cyrys, J., Bellander, T., Lewne, M., & Brunekreef, B.: Estimating Long–Term Average Particulate Air Pollution Concentrations: Application of Traffic Indicators and Geographic Information Systems. Epidemiology, 14 (2), 228–239, 10.1097/01.EDE.0000041910.49046.9B, 2003.

Crawford, J., Ahn, J., Al–Saadi, J., Chang, L., Emmons, L., Kim, J., Lee, G., Park, J., Park, R., Woo, J., Song, C., Hong, J., Hong, Y., Lefer, B., Lee, M., Lee, T., Kim, S., Min, K., Yum, S., Shin, H., Kim, Y., Choi, J., Park, J., Szykman, J., Long, R., Jordan, C., Simpson, I., Fried, A., Dibb, J., Cho, S., and Kim, Y.: The Korea–United States Air Quality (KORUS–AQ) field study. Elementa: Science of the Anthropocene, 9 (1): 00163. https://doi.org/10.1525/elementa.2020.00163, 2021.

Eck, T.F., Holben, B.N., Kim, J., Beyersdorf, A.J., Choi, M., Lee, S., Koo, J. H., Giles, D. M., Schafer, J. S., Sinyuk, Peterson, A. D. A., Reid, J. S., Arola, A., Slutsker, I., Smirnov, A., Sorokin, M., Kraft, J., Crawford, J. H., Anderson, B. E., Thornhill, K. L., Diskin, G., Kim, S. W., Park, S. J.: Influence of cloud, fog, and high relative humidity during pollution transport events in South Korea: Aerosol properties and PM2.5 variability, Atmos. Environ., 232, https://doi.org/10.1016/j.atmosenv.2020.117530, 2020.

Hochadel, M., Heinrich, J., Gehring, U., Morgenstern, V., Kuhlbusch, T., Link, E., Wichmann, H. E., Krämer, U.: Predicting long–term average concentrations of traffic–related air pollutants using GIS–based information, Atmos. Environ., 40, 542–553, https://doi.org/10.1016/j.atmosenv.2005.09.067, 2006.

Hersbach, H., Bell, B., Berrisford, P., Biavati, G., Horányi, A., Muñoz Sabater, J., Nicolas, J., Peubey, C., Radu, R., Rozum, I., Schepers, D., Simmons, A., Soci, C., Dee, D., Thépaut, J–N. (2023): ERA5 hourly data on single levels from 1940 to present. Copernicus Climate Change Service (C3S) Climate Data Store (CDS), https://doi.org/10.24381/cds.adbb2d47 (Accessed on 28–02–2024).

Jordan, C., Crawford, J. H., Beyersdorf, A. J., Eck, T. F., Halliday, H. S., Nault, B. A., Chang, L. S., Park, J. S., Park, R. J., Lee, G. W., Kim, H. J., Ahn, J. Y., Cho, S. J., Shin, H. J., Lee, J. H., Jung, J. S., Kim, D. S., Lee, M. H., Lee, T. H., Whitehill, A., Szykman, J., Schueneman, M. K., Campuzano–Jost, P., Jimenez, J. L., DiGangi, J. P., Diskin, G. S., Anderson, B. E., Moore, R. H., Ziemba, L. D., Fenn, M. A., Hair, J. W., Kuehn, R. E., Holz, R. E., Chen, G., Travis, K., Shook, M., Peterson, D. A., Lamb, K. D., Schwarz, J. P.: Investigation of factors controlling PM2.5 variability across the South Korean Peninsula during KORUS–AQ. Elementa: Science of the Anthropocene, 8, 28, https://doi.org/10.1525/elementa.424, 2020.

Karroum, K., Lin, Y.J., Chiang, Y.Y., Maissa, Y.B., El Haziti, M., Sokolov, A., Delbarre, H.: A Review of Air Quality Modeling. MAPAN, 35, 287–300, https://doi.org/10.1007/s12647-020-00371-8, 2020.

Kim, H., Park, R. J., Kim, S., Brune, W. H., Diskin, G. S., Fried, A., Hall, S. R., Weinheimer, A. J., Wennberg, P., Wisthaler, A., Blake, D. R., and Ullmann, K.: Observed versus simulated OH reactivity during KORUS–AQ campaign: Implications for emission inventory and chemical environment in East Asia. Elementa: Science of the Anthropocene, 10 (1), 00030, https://doi.org/10.1525/elementa.2022.00030, 2022.

Kim, S., Seco, R., Gu, D., Sanchez, D., Jeong, D., Guenther, A., Lee, Y., Mak, J., Su, L., Kim, D., Lee, Y., Ahn, J., Mcgee, T., Sullivan, J., Long, R., Brune, W., Thames, A., Wisthaler, A., Müller, M., Mikoviny, T., Weinheimer, A., Yang, M., Woo, J., Kim, S., Park, H.: The role of a suburban forest in controlling vertical trace gas and OH reactivity distributions – a case study for the Seoul metropolitan area, Faraday Discuss., 226, 537–550, https://doi.org/10.1039/D0FD00081G, 2021.

Lennartson, E., Wang J., Gu J., L. C. Garcia, Ge C., Gao M., Choi M., Saide Peralta, G. Carmichael, Kim J., and Janz S.: Diurnal variation of aerosol optical depth and PM2.5 in South Korea: a synthesis from AERONET, satellite (GOCI), KORUS–AQ observation, and the WRF–Chem model, Atmos. Chem. Phys., 18, 15125–15144, https://doi.org/10.5194/acp-18-15125-2018, 2018.

Matheron, G.: Principles of geostatistics, Econ. Geol., 58 (8), 1246–1266, https://doi.org/10.2113/gsecongeo.58.8.1246, 1963.

Murphy, A, H.: Skill scores based on the mean square error and their relationships to the correlation coefficient, Mon. Wea. Rev., 116, 2417–2424, https://doi.org/10.1175/1520-0493(1988)116<2417:SSBOTM>2.0.CO;2, 1988.

Oak, Y. J., Park, R. J., Schroeder, J. R., Crawford, J. H., Blake, D. R., Weinheimer, A. J., Woo, J., Kim, S., Yeo, H., Fried, A., Wisthaler, A., and Brune, W. H.: Evaluation of simulated O_3 production efficiency during the KORUS–AQ campaign: Implications for anthropogenic NOx emissions in Korea, Elementa: Science of the Anthropocene, 7, 56, https://doi.org/10.1525/elementa.394, 2019.

Park, R. J., Oak, Y. J., Emmons, L. K., Kim, C. H., Pfister, G. G., Carmichael, G. R., Saide, P. E., Cho, S., Kim, S., Woo, J., Crawford, J. H., Gaubert, B., Lee, H., Park, S., Jo, Y., Gao, M., Tang, B., Stanier, C. O., Shin, S., Park, H., Bae, C., and Kim, E: Multi–model intercomparisons of air quality simulations for the KORUS–AQ campaign. Elementa: Science of the Anthropocene, 9 (1), 00139, https://doi.org/10.1525/elementa.2021.00139, 2021.

Peterson, D. A., Hyer, E., Han, S., Crawford J., Park, R. J., Holz, R., Kuehn, R. E., Eloranta, E., Knote, C. J., Jordan, C. E., and Lefer, B.: Meteorology influencing springtime air quality, pollution transport, and visibility in Korea, air quality, pollution transport, and visibility in Korea. Elem Sci, 7, 57, https://doi.org/10.1525/elementa.395, 2019.

Sachse, G. W., Collins, J. E. Jr., Hill, G. F., Wade, L. O., Burney, L. G., and Ritter, J. A.: Airborne tunable diode laser sensor for high–precision concentration and flux measurements of carbon monoxide and methane. In Measurement of atmospheric gases 1433: 157–166. International Society for Optics and Photonics, https://doi.org/10.1117/12.46162, 1991.

Schnell, J. L., Holmes, C. D., Jangam, A., and Prather, M. J.: Skill in forecasting extreme ozone pollution episodes with a global atmospheric chemistry model, Atmos. Chem. Phys., 14, 7721–7739, https://doi.org/10.5194/acp-14-7721-2014, 2014.

Schroeder, J. R., Crawford, J. H., Ahn, J. Y., Chang, L. S., Fried, A. Walega, J. Weinheimer, A., Montzka, D. D., Hall, S. R., Ullmann, K., Wisthaler, A., Mikoviny, T., Chen, G., Blake, D. R., Blake, N. J., Hughes, S. C., Meinardi, S., Diskin, G., Digangi, J. P., Choi, Y. H., Pusede, S. E., Huey, G. L., Tanner, D. J., Kim, M., Wennberg, P.: Observation–based modeling of

437   ozone chemistry in the Seoul metropolitan area during the Korea–United States Air Quality Study (KORUS–AQ). Elementa:

438   Science of the Anthropocene, 8, 3, https://doi.org/10.1525/elementa.400, 2020.

439   Shepard, S.: A two-dimensional interpolation function for irregularly-spaced data, in: Proceedings of the 1968 23rd ACM

440   national conference (ACM '68), Association for Computing Machinery, New York, NY, USA, 517–524,

441   https://doi.org/10.1145/800186.810616, 1968

442   Susaya, J., Kim, K., Shon, Z., and Brown, R.: Demonstration of long–term increases in tropospheric O_3 levels: Causes and

443   potential impacts, Chemosphere, 92, 1520–1528, https://doi.org/10.1016/j.chemosphere.2013.04.017, 2013.

444   Travis, K. R., Crawford, J. H., Chen, G., Jordan, C. E., Nault, B., Kim, H., Jimenez, J. L. Jost, C., Dibb, J., Woo, J. H., Kim,

445   Y., Zhai, S., Wang, X., McDuffie, E., Luo, G., Yu, F., Kim, S., Simpson, I. J., Blake, D. R., Chang, L., Kim, M. J.: Limitations

446   in representation of physical processes prevent successful simulation of PM2.5 during KORUS–AQ, Atmos. Chem. Phys.,

447   https://doi.org/10.5194/acp-22-7933-2022, 2022.

448   Weinheimer, A. J., Walega, J. G., Ridley, B. A., Gary, B. L., Blake, D. R., Blake, N. J., Rowland, F. S., Sachse, G. W.,

449   Anderson, B. E., and Collins, J. E.: Meridional distributions of NOx, NOy, and other species in the lower stratosphere and

450   upper troposphere during AASE II., Geophys. Res. Lett., 21 (23), 2583–2586, https://doi.org/10.1029/94GL01897, 1994.

451   Wilson, C.: KORUS-AQ gridded O3, NOx, and CO observations created using ground station data, Dryad [data set],

452   https://doi.org/10.5061/dryad.sf7m0cgf5, 2024.